IEEE Access
Multidisciplinary | Rapid Review | Open Access Journal

Received January 9, 2019, accepted March 10, 2019, date of publication March 13, 2019, date of current version April 1, 2019.

Digital Object Identifier 10.1109/ACCESS.2019.2904764

Noise Prevention Research in the Hyperbaric Oxygen Chamber by Flux Vector Splitting Format

LIN LI[1], JUNQIANG XI[1], AND REZA LANGARI[2], (Senior Member, IEEE)
[1]School of Mechanical Engineering, Beijing Institute of Technology, Beijing 100081, China
[2]Engineering Technology and Industrial Distribution, Texas A&M University, College Station, TX 77840, USA

Corresponding author: Junqiang Xi (xijunqiang@bit.edu.cn)

This work was supported in part by the China Scholarship Council under Grant 201706030054, and in part by the Beijing Institute of Technology Joint Ph.D. Student Training Scholarship.

ABSTRACT This paper describes the application of computational fluid dynamics(CFD) in noise prevention of hyperbaric oxygen chambers. The flux vector splitting format and matrix transformation are used in the calculation of flow field in the hyperbaric oxygen chamber. At first, this paper simplifies the model of the hyperbaric oxygen chamber, and calculates the conservative state equation by flux vector splitting format. Being auxiliary to initial conditions, boundary conditions, meshing, time steps, and other computing elements, this paper gets the transient distribution of the parameters of each time step from flowing start to its near stop. Through displaying the data by graphic, we get the flow velocity variation, the location of the shock wave, the variational trend of pressure, and the variational trend of temperature. This paper compares the numerical and experimental results. Their similarity degree is high and this proves the feasibility to design Low-noise hyperbaric oxygen chamber by this numerical calculation method.

INDEX TERMS Flux vector splitting format, hyperbaric oxygen chamber, computational fluid dynamics (CFD), noise analysis, cabin experiment.

I. INTRODUCTION

The hyperbaric chamber is a medical device that treats diseases in a closed compartment filled with oxygen or compressed air which is one atmosphere higher than standard atmospheric pressure. The hyperbaric chamber produces noise during operation and use, and the noise adversely affects the health of the patient in the hyperbaric chamber. The attenuation of this noise is usually performed through installing silencers at the air inlet. In order to characterize the attenuation capacity of the silencers and to verify that the air flow is the most significant source of noise, a series of noise measurements is presented. Experiments are carried out in the open field by emptying a pressurized tank in various conditions of opening the exhaust valve for different types of silencers placed at the outlet [1]. To cut the cost of the experiment, engineers and technicians use CFD calculation software to help their designing in recent years [2]–[4]. Kuan and Huang discusses the noise distribution of blower flow field. The periodic pressure output value is calculated by CFD in the input of sound pressure field to simulate the aerodynamic [5]. Marsan *et al.* [6] present study aims at identifying the noise generation mechanisms in a radial blower in order to suggest simple structure modifications to reduce the noise. But, these CFD softwares cannot meet their needs on designing in some degree. For example, the author of this paper once tried to use one CFD software to design hyperbaric oxygen chamber. But, the algorithm in this software cannot capture the shock wave in the cabin. Liu and Ji [7] used a 3D time-domain computational fluid dynamics (CFD) approach to calculate the acoustic attenuation performance of perforated tube silencers. However, in practical applications, the use of silencers does not provide satisfactory noise reduction effects. During the design phase of the hyperbaric chamber, there is a need for a method that can reduce cabin noise.

At present, for different physical models, often have different calculation methods. The Flux Vector Splitting Format was used in many research hotspots [8], [9]. This format is calculated by a strong dissipative guarantee, which can capture the shock wave generated by supersonic flow in the absence of artificial viscosity. The flux vector split format is a first-order upwind format, and its calculation speed is fast. It can take up limited computational resources to carry

The associate editor coordinating the review of this manuscript and approving it for publication was Guiwu Wei.

out the transient calculation of the whole working condition. For the newest research on the flux vector splitting format, Tokareva, SA and Toro, EF extend the Toro-Vazquez flux vector splitting approach (TV), originally proposed for the ideal 1D Euler equations, to the Baer-Nunziato equations of compressible two-phase flow [10]. A new scheme of arbitrary high order accuracy in both space and time is proposed to solve hyperbolic conservative laws, based on the idea of the flux vector splitting (FVS) in literature [11]. To achieve a parameter-free upwind scheme capable of simulating all speeds accurately and efficiently, QU Feng, YAN Chao, SUN Di and YUAN Wu present a new upwind scheme called AUSMPWM in literature [12]. This scheme computes the numerical mass flux as the AUSMPW+ and computes the interfacial sound speed in a different way. Also, it computes the pressure flux by limiting the dissipation if the Mach number is less than 1. In addition, the literature [13] extends the original approach to the compressible Navier-Stokes equations considering flux vector splitting schemes and viscous wall boundary conditions at the immersed geometry. In literature [14], Nonlinear aero elasticity is studied by an improved CFD and CSD coupled program. An AUSMpw+ flux splitting scheme, combined with an implicit time marching technology and geometric conservation law, is utilized to solve unsteady aerodynamic pressure; The finite element corotational theory is applied to model geometrically nonlinear two-dimensional and three-dimensional panels, and a predictor-corrector program with an approximately energy conservation is developed to obtain nonlinear structure response. From these flux vector splitting format's application, we know that this calculation format is very suitable for calculating the state equation for solving the compressible supersonic internal flow field model of hyperbaric oxygen chamber.

The purpose of this paper is to reveal the parameters' variation in the whole flow field of the hyperbaric oxygen chamber during air flowing and to explore the source of the noise. It provide a method for designing a more comfortable hyperbaric chamber. The mathematical model and the numerical calculation can meet the requirement of research on hyperbaric oxygen chamber and save the experimental cost. In this paper, we try to solve the state equation of fluid model by numerical method. The results of the calculation are approximation of real flow with a certain precision. Finally, the correctness of the mathematical model is verified by experiments. The research methods provided in this article can help engineers and technicians to design more comfortable and intelligent hyperbaric chamber for medical or other uses at a low cost.

The innovations in this paper are stated below. First, the flux vector splitting format is used to study the noise problem in the hyperbaric oxygen chamber. Second, this paper reduces the computational domain from 3D to 2D to improve computational efficiency. Third, the authors deduced the transformation matrixs T^{-1}, T, P^{-1}, P for matrix transformation of FVS.

The rest of the paper is organized as follows. Simplified physical model is presented in Section II. The detailed mathematical model is theoretically derived in Section III. Calculation results of the mathematical model are analyzed in Section IV. Then, an experiment is provided and a comparison is conducted between the experimental and computational results in Section V, followed by conclusion.

II. PHYSICAL MODEL

The physical model of the hyperbaric chamber consists of a high pressure source (gas tank), a pipe, a valve and a cabin. The simplified model is shown in Figure 1. The working principle of the hyperbaric chamber is described as follows. When the person enters the cabin 3 on the right side of Figure 1, the solenoid valve 2 is opened to connect the gas tank 1 and the cabin 3 until the cabin 3's pressure reaches the set value.

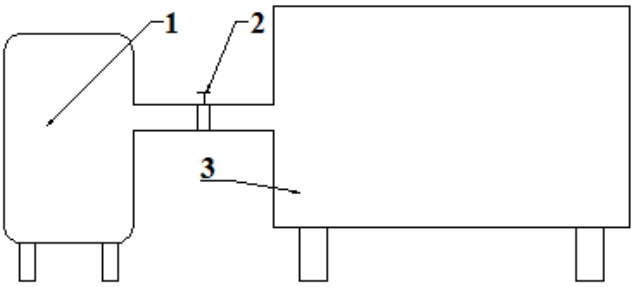

FIGURE 1. Simplified physical model of hyperbaric oxygen chamber.

Figure 1 has two confined spaces. 1 represents the high pressure source (gas tank), 3 represents the functional area of the cabin. They are connected through a pipe. And valve 2 controls the connection and truncation between them. Assume that the model as a whole is adiabatic. Assume that the gas tank 1 is large enough and the pressure is constant in the tank. Assume that the valve is momentarily open and reaches the same diameter as the pipe. Assume that the gas is the ideal gas in the model.

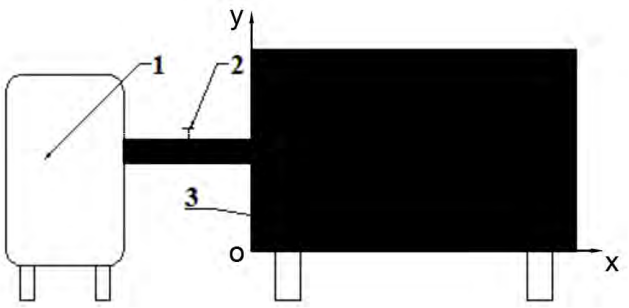

FIGURE 2. Calculation area diagram of the mathematical model.

Take the dark part of Figure 2 as the calculation field. Because it can be seen as that the dark area made the volume of the entire cabin by scanning 180 degrees around the axis

of the pipeline. This dark area is symmetrical about the pipe axis. Take the bottom of the oxygen chamber, which parallel to the pipeline, as the x-axis. And, take radial direction for the y-axis to establish the coordinate system, shown as Figure 2.

III. MATHEMATICAL MODEL

Mathematical model is used to solve the state equation of ideal gas flow by flux vector splitting algorithm. Finite difference expressions are established. According to the simplified model of the hyperbaric chamber, the initial condition, the boundary condition and the time step, the author programmed to solve the parameters' change of the flow field.

A. CONTROL EQUATIONS OF AIR FLOW

Select the non-viscous flow equation (Euler equation) as the state equation model. Ignoring the influence of gravity and electric field force in the model. At the same time, due to the adiabatic model, the volume heat is neglected, such as the absorption and dissipation of radiant heat. Ignore the temperature gradient where heat transfers through the surface (heat conduction). The conservation state equations are expressed as follows [15]:

Continuity equation:

$$\frac{\partial \rho}{\partial t} + \rho \frac{\partial u}{\partial x} + \rho \frac{\partial v}{\partial y} = 0 \tag{1}$$

Momentum equation:

$$\frac{\partial \rho u}{\partial t} + \frac{\partial \rho u^2}{\partial x} + \frac{\partial \rho uv}{\partial y} = -\frac{\partial p}{\partial x} \tag{2}$$

$$\frac{\partial \rho u}{\partial t} + \frac{\partial \rho uv}{\partial x} + \frac{\partial \rho v^2}{\partial y} = -\frac{\partial p}{\partial y} \tag{3}$$

Energy equation:

$$\frac{\partial}{\partial t}[\rho(e + \frac{\overrightarrow{V}^2}{2})] + \frac{\partial}{\partial x}[\rho(e + \frac{\overrightarrow{V}^2}{2})u] + \frac{\partial}{\partial y}[\rho(e + \frac{\overrightarrow{V}^2}{2})v] = -\frac{\partial up}{\partial x} - \frac{\partial vp}{\partial y} \tag{4}$$

The thermal relationship of the ideal gas with specific heat at constant volume is listed as follows [16]:

$$e = c_v T \tag{5}$$

$$c_v = \frac{1}{\gamma - 1} R \tag{6}$$

$$c^2 = \gamma RT \tag{7}$$

As well as the state equation of the ideal gas:

$$p = \rho RT \tag{8}$$

The total energy is equal to the sum of internal energy and kinetic energy:

$$E = e + \frac{\overrightarrow{V}^2}{2} \tag{9}$$

where the specific heat ratio $\gamma = \frac{c_p}{c_v}$, for the standard state of the air $\gamma = 1.4$, c_p is specific heat capacity at constant pressure, and c_v is specific heat capacity at constant volume. R is the gas constant, at room temperature and pressure, generally take $R = 287J/(kg * K)$. ρ is the gas density, T is the gas temperature, and p is the pressure. u is the velocity of the gas flow in the x direction. v is the velocity of the gas flow in the y direction. $\overrightarrow{V}$ represents the total velocity vector. c represents the speed of sound.

B. JACOBIAN MATRIX OF CONTROL EQUATIONS

The equations (1) to (8) can be abbreviated as follows:

$$\left\{ \begin{array}{l} \frac{\partial U_1}{\partial t} + \frac{\partial F_1}{\partial x} + \frac{\partial G_1}{\partial y} = 0 \\ \frac{\partial U_2}{\partial t} + \frac{\partial F_2}{\partial x} + \frac{\partial G_2}{\partial y} = 0 \\ \frac{\partial U_3}{\partial t} + \frac{\partial F_3}{\partial x} + \frac{\partial G_3}{\partial y} = 0 \\ \frac{\partial U_4}{\partial t} + \frac{\partial F_4}{\partial x} + \frac{\partial G_4}{\partial y} = 0 \end{array} \right\} \tag{10}$$

in which, $U_1 = \rho$, $U_2 = \rho u$, $U_3 = \rho v$, $U_4 = \rho E$; $F_1 = \rho u$, $F_2 = p + \rho u^2$, $F_3 = \rho uv$, $F_4 = \rho Eu$; $G_1 = \rho v$, $G_2 = \rho uv$, $G_3 = p + \rho v^2$, $G_4 = \rho Ev + pv$; And then simplified as:

$$\frac{\partial \overrightarrow{U}}{\partial t} = -\frac{\partial \overrightarrow{F}}{\partial x} - \frac{\partial \overrightarrow{G}}{\partial y} \tag{11}$$

in which, $\overrightarrow{U} = [U_1\ U_2\ U_3\ U_4]^{\mathrm{T}}$, $\overrightarrow{F} = [F_1\ F_2\ F_3\ F_4]^{\mathrm{T}}$, $\overrightarrow{G} = [G_1\ G_2\ G_3\ G_4]^{\mathrm{T}}$ Equation (11) can be changed to:

$$\frac{\partial \overrightarrow{U}}{\partial t} = -\frac{\partial \overrightarrow{F}}{\partial \overrightarrow{U}} \frac{\partial \overrightarrow{U}}{\partial x} - \frac{\partial \overrightarrow{G}}{\partial \overrightarrow{U}} \frac{\partial \overrightarrow{U}}{\partial y} \tag{12}$$

$\frac{\partial \overrightarrow{F}}{\partial \overrightarrow{U}}$ and $\frac{\partial \overrightarrow{G}}{\partial \overrightarrow{U}}$ are called the Jacobian matrix of flux vector F and G respectively, abbreviated as A and B. So equation (12) can be written as:

$$\frac{\partial \overrightarrow{U}}{\partial t} = -A\frac{\partial \overrightarrow{U}}{\partial x} - B\frac{\partial \overrightarrow{U}}{\partial y} \tag{13}$$

For this model, the Jacobian matrix A and B are described as equation (14) (15), as shown at the top of the next page, [17]: among them: $E = (e + \frac{\overrightarrow{V}^2}{2}) = (\frac{c^2}{\gamma(\gamma-1)} + \frac{\overrightarrow{V}^2}{2})$

C. FLUX VECTOR SPLITTING SCHEME

The matrix **A** and the matrix **B** are diagonalized in equations (16) and (17) as follows:

$$T^{-1}AT = \begin{bmatrix} \lambda_{a_1} & 0 & 0 & 0 \\ 0 & \lambda_{a_2} & 0 & 0 \\ 0 & 0 & \lambda_{a_3} & 0 \\ 0 & 0 & 0 & \lambda_{a_4} \end{bmatrix} \tag{16}$$

$$P^{-1}BP = \begin{bmatrix} \lambda_{b_1} & 0 & 0 & 0 \\ 0 & \lambda_{b_2} & 0 & 0 \\ 0 & 0 & \lambda_{b_3} & 0 \\ 0 & 0 & 0 & \lambda_{b_4} \end{bmatrix} \tag{17}$$

where λ_{a_1} λ_{a_2} λ_{a_3} λ_{a_4} and λ_{b_1} λ_{b_2} λ_{b_3} λ_{b_4} are the eigenvalues of **A** and **B** respectively. T^{-1} and T, P^{-1} and P are listed as Equation (18) (19) (20) (21), as shown at the top of the next page.

$$A = \begin{bmatrix} 0 & 1 & 0 & 0 \\ -u^2 + \frac{\gamma-1}{2}\vec{V}^2 & (3-\gamma)u & (1-\gamma)v & \gamma-1 \\ -uv & v & u & 0 \\ -u[\gamma E - (\gamma-1)\vec{V}^2] & \gamma E - \frac{\gamma-1}{2}(\vec{V}^2 + 2u^2) & (1-\gamma)uv & \gamma u \end{bmatrix} \tag{14}$$

$$B = \begin{bmatrix} 0 & 0 & 1 & 0 \\ -uv & v & u & 0 \\ -v^2 + \frac{\gamma-1}{2}\vec{V}^2 & (1-\gamma)u & (3-\gamma)v & \gamma-1 \\ -v[\gamma E - (\gamma-1)\vec{V}^2] & (1-\gamma)uv & \gamma E - \frac{\gamma-1}{2}(\vec{V}^2 + 2v^2) & \gamma v \end{bmatrix} \tag{15}$$

$$T^{-1} = \begin{bmatrix} 1 - \frac{\gamma-1}{2}\frac{u^2+v^2}{c^2} & \frac{(\gamma-1)u}{c^2} & \frac{(\gamma-1)v}{c^2} & \frac{1-\gamma}{c^2} \\ \frac{v}{\rho} & 0 & -\frac{1}{\rho} & 0 \\ \frac{c}{\rho}(\frac{\gamma-1}{2}\frac{u^2+v^2}{c^2} - \frac{u}{c}) & \frac{1-\frac{(\gamma-1)u}{c}}{\rho} & \frac{(1-\gamma)v}{c\rho} & \frac{\gamma-1}{c\rho} \\ \frac{c}{\rho}(\frac{\gamma-1}{2}\frac{u^2+v^2}{c^2} + \frac{u}{c}) & -\frac{1+\frac{(\gamma-1)u}{c}}{\rho} & \frac{(1-\gamma)v}{c\rho} & \frac{\gamma-1}{c\rho} \end{bmatrix} \tag{18}$$

$$T = \begin{bmatrix} 1 & 0 & \frac{\rho}{2c} & \frac{\rho}{2c} \\ u & 0 & \frac{\rho}{2c}(u+c) & \frac{\rho}{2c}(u-c) \\ v & -\rho & \frac{\rho}{2c}v & \frac{\rho}{2c}v \\ \frac{u^2+v^2}{2} & -\rho v & \frac{\rho}{2c}(\frac{u^2+v^2}{2} + \frac{c^2}{\gamma-1} + cu) & \frac{\rho}{2c}(\frac{u^2+v^2}{2} + \frac{c^2}{\gamma-1} - cu) \end{bmatrix} \tag{19}$$

$$P^{-1} = \begin{bmatrix} 1 - \frac{\gamma-1}{2}\frac{u^2+v^2}{c^2} & \frac{(\gamma-1)u}{c^2} & \frac{(\gamma-1)v}{c^2} & \frac{1-\gamma}{c^2} \\ -\frac{u}{\rho} & \frac{1}{\rho} & 0 & 0 \\ \frac{c}{\rho}(\frac{\gamma-1}{2}\frac{u^2+v^2}{c^2} - \frac{v}{c}) & \frac{0-\frac{(\gamma-1)u}{c}}{\rho} & \frac{1-\frac{(\gamma-1)v}{c}}{\rho} & \frac{\gamma-1}{c\rho} \\ \frac{c}{\rho}(\frac{\gamma-1}{2}\frac{u^2+v^2}{c^2} + \frac{v}{c}) & -\frac{0+\frac{(\gamma-1)u}{c}}{\rho} & -\frac{1+\frac{(\gamma-1)v}{c}}{\rho} & \frac{\gamma-1}{c\rho} \end{bmatrix} \tag{20}$$

$$P = \begin{bmatrix} 1 & 0 & \frac{\rho}{2c} & \frac{\rho}{2c} \\ u & \rho & \frac{\rho}{2c}u & \frac{\rho}{2c}u \\ v & 0 & \frac{\rho}{2c}(v+c) & \frac{\rho}{2c}(v-c) \\ \frac{u^2+v^2}{2} & \rho u & \frac{\rho}{2c}(\frac{u^2+v^2}{2} + \frac{c^2}{\gamma-1} + cv) & \frac{\rho}{2c}(\frac{u^2+v^2}{2} + \frac{c^2}{\gamma-1} - cv) \end{bmatrix} \tag{21}$$

Establish:

$$[\lambda_a{}^+] = \begin{bmatrix} \frac{\lambda_{a_1}+|\lambda_{a_1}|}{2} & 0 & 0 & 0 \\ 0 & \frac{\lambda_{a_2}+|\lambda_{a_2}|}{2} & 0 & 0 \\ 0 & 0 & \frac{\lambda_{a_3}+|\lambda_{a_3}|}{2} & 0 \\ 0 & 0 & 0 & \frac{\lambda_{a_4}+|\lambda_{a_4}|}{2} \end{bmatrix} \tag{22}$$

$$[\lambda_a{}^-] = \begin{bmatrix} \frac{\lambda_{a_1}-|\lambda_{a_1}|}{2} & 0 & 0 & 0 \\ 0 & \frac{\lambda_{a_2}-|\lambda_{a_2}|}{2} & 0 & 0 \\ 0 & 0 & \frac{\lambda_{a_3}-|\lambda_{a_3}|}{2} & 0 \\ 0 & 0 & 0 & \frac{\lambda_{a_4}-|\lambda_{a_4}|}{2} \end{bmatrix} \tag{23}$$

$$[\lambda_b{}^+]=\begin{bmatrix} \frac{\lambda_{b_1}+|\lambda_{b_1}|}{2} & 0 & 0 & 0 \\ 0 & \frac{\lambda_{b_2}+|\lambda_{b_2}|}{2} & 0 & 0 \\ 0 & 0 & \frac{\lambda_{b_3}+|\lambda_{b_3}|}{2} & 0 \\ 0 & 0 & 0 & \frac{\lambda_{b_4}+|\lambda_{b_4}|}{2} \end{bmatrix} \tag{24}$$

$$[\lambda_b{}^-]=\begin{bmatrix} \frac{\lambda_{b_1}-|\lambda_{b_1}|}{2} & 0 & 0 & 0 \\ 0 & \frac{\lambda_{b_2}-|\lambda_{b_2}|}{2} & 0 & 0 \\ 0 & 0 & \frac{\lambda_{b_3}-|\lambda_{b_3}|}{2} & 0 \\ 0 & 0 & 0 & \frac{\lambda_{b_4}-|\lambda_{b_4}|}{2} \end{bmatrix} \tag{25}$$

where: $[\lambda_a{}^+]$ is the set of all positive eigenvalues of matrix A. $[\lambda_a{}^-]$ is a set of all negative eigenvalues of matrix A. $[\lambda_b{}^+]$ is the set of all positive eigenvalues of matrix B. $[\lambda_b{}^-]$ is a set of all negative eigenvalues of matrix B.

The eigenvalues in the characteristic equations of the hyperbaric chamber model are: $\lambda_{a_1} = u, \lambda_{a_2} = u, \lambda_{a_3} = u+c, \lambda_{a_4} = u-c, \lambda_{b_1} = v, \lambda_{b_2} = v, \lambda_{b_3} = v+c, \lambda_{b_4} = v-c$. We have:

$$\left\{\begin{array}{l} A^+ = T^{-1}[\lambda_a{}^+]T \\ A^- = T^{-1}[\lambda_a{}^-]T \\ B^+ = P^{-1}[\lambda_b{}^+]P \\ B^- = P^{-1}[\lambda_b{}^-]P \end{array}\right\} \tag{26}$$

Then we find:

$$\frac{\partial \overrightarrow{U}}{\partial t} = -\frac{A^+\partial \overrightarrow{U}}{\partial x} - \frac{A^-\partial \overrightarrow{U}}{\partial x} - \frac{B^+\partial \overrightarrow{U}}{\partial y} - \frac{B^-\partial \overrightarrow{U}}{\partial y} \tag{27}$$

For inviscid flow, F and G can be expressed directly by Jacobian matrix transform:

$$\left\{\begin{array}{l} F = AU \\ G = BU \end{array}\right\} \tag{28}$$

so we have:

$$\frac{\partial \overrightarrow{U}}{\partial t} = -\frac{\partial \overrightarrow{F}^+}{\partial x} - \frac{\partial \overrightarrow{F}^-}{\partial x} - \frac{\partial \overrightarrow{G}^+}{\partial y} - \frac{\partial \overrightarrow{G}^-}{\partial y} \tag{29}$$

F^+, G^+ are the flux toward positive direction of the axis. They are only related to the upstream flow information of the axis. Thus, $\frac{\partial \overrightarrow{F}^+}{\partial x}$ and $\frac{\partial \overrightarrow{G}^+}{\partial y}$ should be replaced by backward differences. Similarly, F^-, G^- have the negative flux toward negative direction of the axis. It is only related to the downstream flow information of the axis. Thus $\frac{\partial \overrightarrow{F}^-}{\partial x}$ and $\frac{\partial \overrightarrow{G}^-}{\partial y}$ should be replaced by forward differentials. Thus, the following update rule of the flux vector $\overrightarrow{U}$ is obtained:

$$\begin{aligned} \frac{\partial \overrightarrow{U}}{\partial t} = &-\frac{\overrightarrow{F(i,j)}^+ - \overrightarrow{F(i-1,j)}^+}{\Delta x} - \frac{\overrightarrow{F(i+1,j)}^- - \overrightarrow{F(i,j)}^-}{\Delta x} \\ &- \frac{\overrightarrow{G(i,j)}^+ - \overrightarrow{G(i,j-1)}^+}{\Delta y} - \frac{\overrightarrow{G(i,j+1)}^- - \overrightarrow{G(i,j)}^-}{\Delta y} \end{aligned} \tag{30}$$

$$\overrightarrow{U(t)} = \overrightarrow{U(t-1)} + \frac{\partial \overrightarrow{U}}{\partial t}\Delta t \tag{31}$$

Among them, Δx, Δy, Δt will be introduced in sections 2.4 and 2.7 respectively. Repeatedly use the newly obtained and the original variable: u, v, T in formulas (26) to (31). And this is the flux vector splitting numerical calculation method forwarded in time.

D. GRID DIVISION

Refer to the actual hyperbaric oxygen chamber size, divided grid. As shown in Figure 2, take pipe axis for the x axis. Take the intersection between the pipeline axis and gas tank's interface as the origin. Take the x-axis positive direction towards the cabin. Divide the x-axis into 205(x) steps on equal length. The length of each step is equal and counted as Δx. Similarly, take the direction, which is perpendicular to x-axis, as the y-axis. The positive direction of the y-axis is away from the origin. Divide the into 130(y) steps on equal length. The length of each step is equal, counted as Δy. They can be calculated by the actual size of the oxygen chamber. For this model, take:

$$\left\{\begin{array}{l} \Delta x = 40mm \\ \Delta y = 40mm \end{array}\right\} \tag{32}$$

E. INITIAL CONDITIONS SETTING

The initial condition is the method of assigning the initial approximation of the grid points in all the calculation fields before the start of the numerical calculation. According to the physical model specified in the second chapter of this paper and the grid division of section 3.4, preset the grid points, which represent the pipe part $\left\{\begin{array}{l} x = 1 \sim 5 \\ y = 62 \sim 71 \end{array}\right\}$, $u = 170\,m/s$, in the x-axis direction, and $v = 0\ m/s$ in y-axis direction. Preset pressure is 2.02×10^5 Pa, the temperature is $288K$. For the grid points representing the cabin $\left\{\begin{array}{l} x = 6 \sim 206 \\ y = 1 \sim 132 \end{array}\right\}$, preset the flow speed to 0 along both the x-axis and y-axis. The pressure is 1.01×10^5 Pa, the temperature is $288K$.

F. BOUNDARY CONDITIONS HANDLING

Set: $P_0 = 2.02 \times 10^5\ Pa$, $T_0 = 288K$

1) INFLOW BOUNDARY CONDITIONS

Let the points $\left\{\begin{array}{l} x = 1 \\ y = 63 \sim 70 \end{array}\right\}$ satisfy the inflow boundary condition:

$$\left\{\begin{array}{l} p = P_0 \\ T = T_0 \\ u(1,j) = (u(2,j) + u(1,j+1) + u(1,j-1))/3 \\ v(1,j) = (v(2,j) + v(1,j+1) + v(1,j-1))/3 \end{array}\right\} \tag{33}$$

2) WALL BOUNDARY CONDITIONS

The physical entity of the model can be seen as the calculation field rotated 180 degrees around the pipe axis. Except the inflow boundary, all of the boundaries in this model can be considered to be wall boundary conditions.

On wall boundary conditions, the pressure condition is the average of the three grid points around it. And, the velocity of the fluid which is perpendicular to the wall surface is set to zero. Taking the wall boundary condition of the points $\begin{Bmatrix} x = 7 \sim 205 \\ y = 1 \end{Bmatrix}$ as an example:

$$\begin{Bmatrix} p(i,1) = (p(i,2) + p(i+1,1) + p(i-1,1))/3 \\ T = T_0 \\ u(1,j) = (u(i,2) + u(i+1,1) + u(i-1,1))/3 \\ v(i,1) = 0 \end{Bmatrix} \quad (34)$$

3) SPECIAL GRID POINTS

Special grid points are the intersection between the inflow boundary condition and the wall boundary conditions. Also, the intersection between the wall boundary conditions and the wall boundary conditions. A total of 8 points are shown in Figure 3:

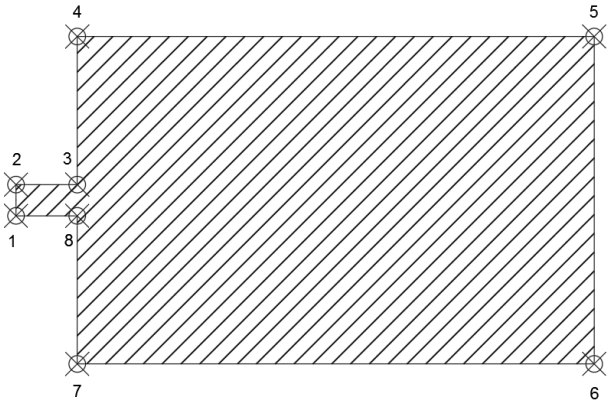

FIGURE 3. Special grid points.

Similarly, the boundary conditions of special grid points are different. The pressure at the grid points 1 and 2 connected to the inflow boundary are both constant P_0, and their velocity v in the y-axis direction is zero. For the velocity of the grid point 3 and 8, the velocity u in the x-axis direction and the velocity v in the y-axis direction are the average values of the grid points around it. For the velocity of the grid points (4, 5, 6, 7), the velocity u in the x-direction and the velocity v in y-direction are all 0, and their pressure are the average values of their surrounding grid points and their own values. As examples, boundary conditions of the grid points (1, 3, 6) are listed as follows:

$$\begin{Bmatrix} p(1,62) = P_0 \\ T(1,62) = T_0 \\ u(1,62) = (u(2,62) + u(1,63) + u(1,62))/3 \\ v(1,62) = 0 \end{Bmatrix} \quad (35)$$

$$\begin{Bmatrix} p(6,71) = (p(5,71)+p(7,71)+p(6,72)+p(6,70))/4 \\ T(6,71) = T_0 \\ u(6,71) = (u(5,71)+u(7,71)+u(6,72)+u(6,70))/4 \\ v(6,71) = (v(5,71)+v(7,71)+v(6,72)+v(6,70))/4 \end{Bmatrix} \quad (36)$$

$$\begin{Bmatrix} p(206,1) = (p(206,2)+p(205,1)+p(206,1))/3 \\ T(206,1) = T_0 \\ u(206,1) = 0 \\ v(206,1) = 0 \end{Bmatrix} \quad (37)$$

G. TIME STEPS CALCULATION

It requires that the time step of each grid point be calculated in turn; and then, the minimum value is taken. For any grid point, its time step (Δ_t) is calculated as [18]:

$$\begin{Bmatrix} \Delta_{tx} = \dfrac{C\Delta_x}{c + \sqrt{u^2}} \\ \Delta_{ty} = \dfrac{C\Delta_y}{c + \sqrt{v^2}} \\ \Delta_t = min(\Delta_{tx}, \Delta_{ty}) \end{Bmatrix} \quad (38)$$

C is the Courant Number. For this model, C is 0.3. Please see section 3.4 grid division about Δ_x and Δ_y. c represents the local speed of sound. The formula is described as follows [17]:

$$c = \sqrt{\gamma RT} \quad (39)$$

T represents the temperature at the grid point. R is the gas constant. γ is the specific heat ratio.

IV. CALCULATION RESULTS AND ANALYSIS

The author has used Matlab for programming calculations, and took the calculate data of three time steps (713, 6554, 70813) to show the change of flow field and the calculation results.

Figure 4 $\sim$ 8 is the parameters distribution in the 713th time step (0.0123s) in the whole flow field.

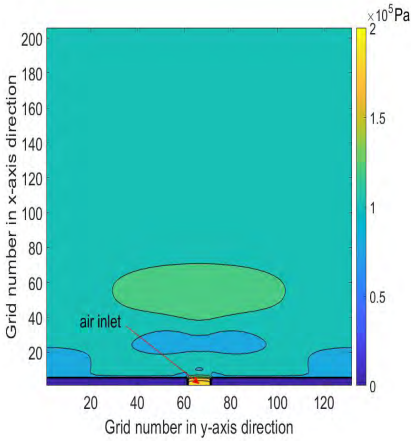

FIGURE 4. Pressure distribution of 713th time steps.

Figure 9 $\sim$ 11 is the parameters distribution in the 6554th time steps (0.1143s) throughout the flow field.

Figure 12 $\sim$ 14 is the parameters distribution in the 70813th time step (2.0798s) throughout the flow field.

From the results of numerical calculation, the algorithm can capture the parameters transient distribution of each time step from flowing start to its near stop, see Figures 4 to 14.

Near the entrance of the oxygen chamber, it can be seen that the velocity u reaches supersonic levels at the 713-time

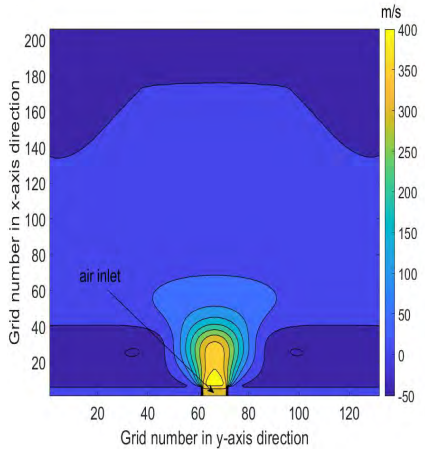

FIGURE 5. Velocity u distribution of 713th time steps.

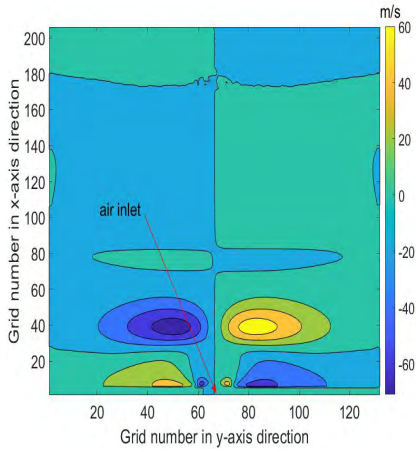

FIGURE 6. Velocity v distribution of 713th time steps.

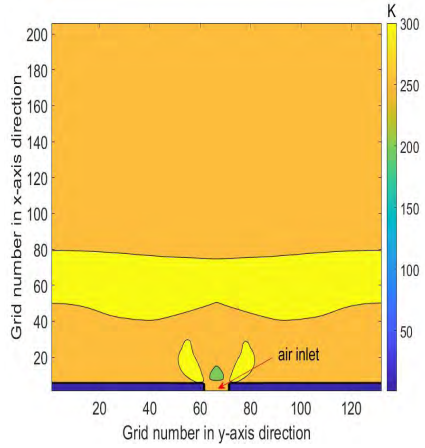

FIGURE 7. Temprature distribution of 713th time steps.

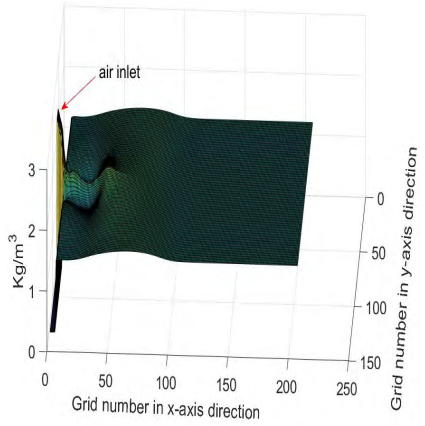

FIGURE 8. Density distribution of 713th time steps.

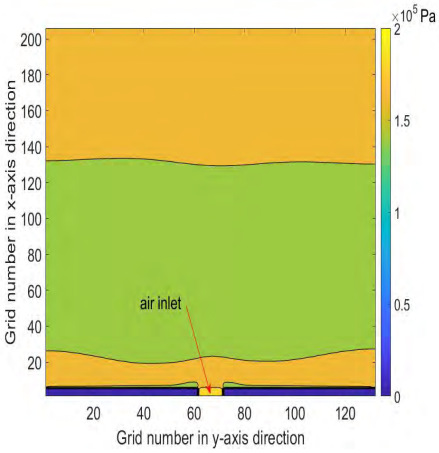

FIGURE 9. pressure distribution of 6554th time steps.

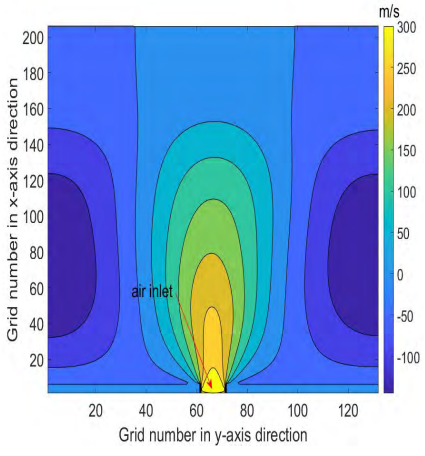

FIGURE 10. Velocity u distribution of 6554th time steps.

step (0.0123s), shown in Figure 5. Meanwhile, at 713 time steps (0.0123s), there appears an area which is less than one atmospheric pressure (light blue area) at the entrance of the oxygen chamber as shown in Figure 4. And, the flow field surrounding the light blue region (light green and yellow areas) is higher than one atmosphere pressure. They have a difference maximum to one atmosphere pressure. This shows a strong fluctuation at the entrance. We know that supersonic air flow can produce shock waves. And shock waves can

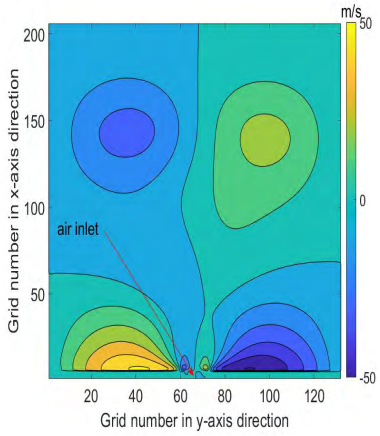

FIGURE 11. Velocity v distribution of 6554th time steps.

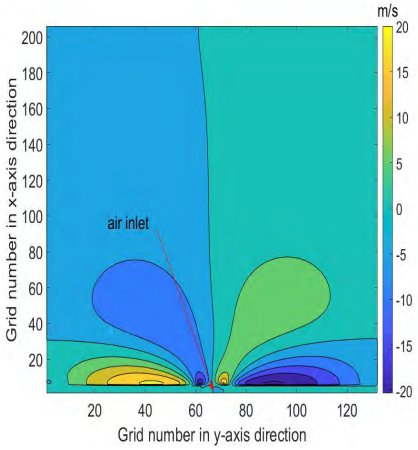

FIGURE 14. Velocity v distribution of 70813th time steps.

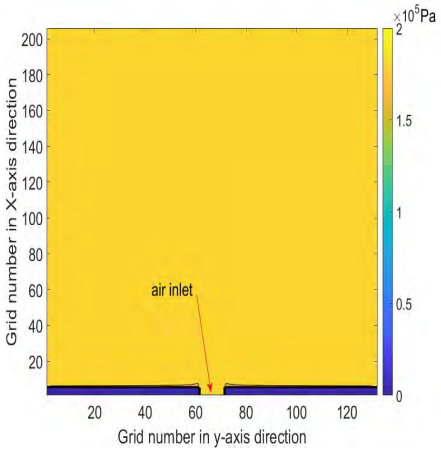

FIGURE 12. Pressure distribution of 70813th time steps.

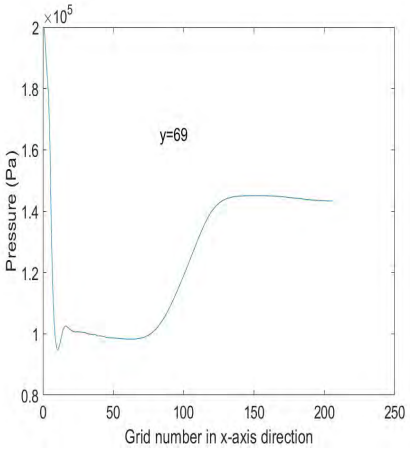

FIGURE 15. Pressure variational curve of 2415th time steps.

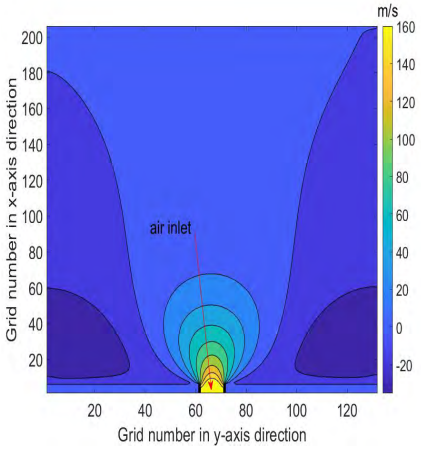

FIGURE 13. velocity u distribution of 70813th time steps.

produce high noise levels. As a matter of fact, the strong fluctuation mentioned above is where shock wave is located. It is where noise mainly comes from in hyperbaric oxygen chamber. Engineers and technicians should try to avoid this strong fluctuation in their hyperbaric oxygen chamber designing. Figure 6 shows the velocity in the radial direction. The image reflects the presence of vortices at the entrance. Figures 7–8 show the variation in temperature and density in the flow field.

At 6554 time-step (0.1143s), as shown in Figure 9, a high pressure region is formed opposite to the intake port near the wall of the oxygen chamber. This shows that the wall obstructs air's high-speed flow and cause a slowdown in congestion. The accumulation of airflow leads to a rise in pressure. At this time step (6554) (0.1143s), as shown in Figures 10–11, the entire flow field forms a large vortex from the distribution of the flow rate.

At 70813 time steps (2.0798s), the pressure of the entire flow field is close to a steady value, as shown in Figure 12. There is no obvious fluctuation in the flow field. There is also a small flow rate near the entrance of the oxygen chamber, as shown in Figures 13–14. The flow is close to stop.

The pressure p, the velocity u which towards the positive direction of x-axis, the velocity v which towards the radial direction of x-axis, and the temperature are showed

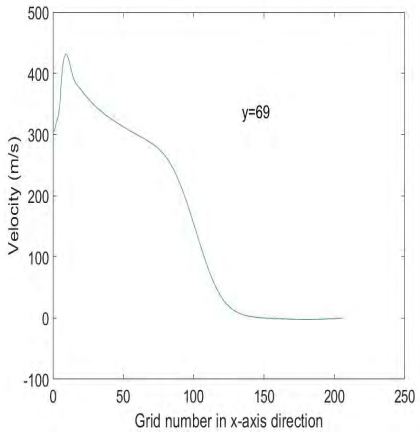

FIGURE 16. Velocity u variational curve of 2415th time steps.

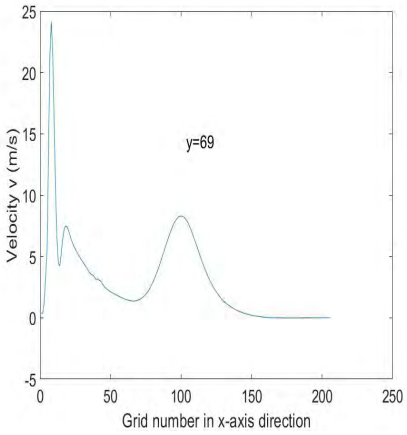

FIGURE 17. Velocity v variational curve of 2415th time steps.

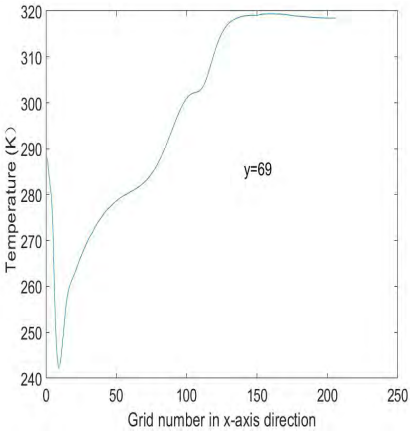

FIGURE 18. Temperature variational curve of 2415th time steps.

in Figures 15–18. In Figure 16, the velocity u exceeds 400 m/s on the y = 69 axis near the entrance of the oxygen chamber at 2415-time step (0.0395s). This speed is greater than the sound speed (340m/s). These parameters show step fluctuation at the location near the entrance of the oxygen chamber. It can be judged that the shock wave is at this step fluctuation position

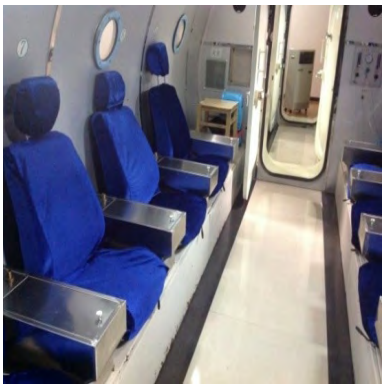

FIGURE 19. Hyperbaric chamber experiments.

FIGURE 20. Pressure sensor PAA-23/25.

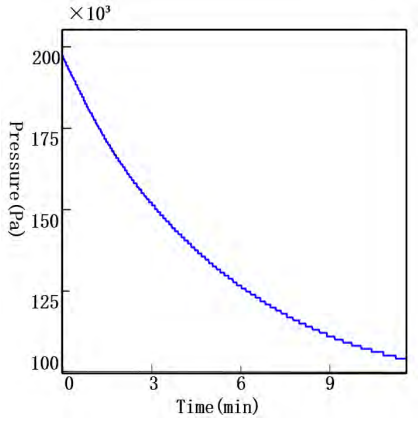

FIGURE 21. The degassing process pressure variational curve during the experiment.

at this time. From the figures 15–18, other fluctuations can also be seen on the axis y = 69. These fluctuations are caused by the combined action of the swell wave and the reflected wave from the wall.

V. EXPERIMENT

The authors made a hyperbaric chamber experiment as shown in Figure 19. The method is to pressurize the hyperbaric chamber to two atmospheres (2.02×10^5 *Pa*) and then

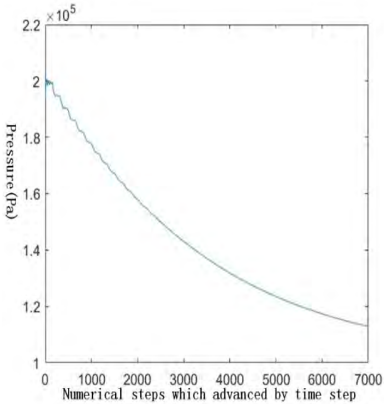

FIGURE 22. Pressure change curve of degassing process during 7000 time steps (1.3401s) by numerical computation.

FIGURE 23. Part of the pipeline diagram of hyperbaric oxygen chamber.

control the bleed valve open. And, record the pressure change curve in the cabin. Select pressure sensor PAA-23/25 (see Figure 20) to measure the pressure change at a point in the cabin. The sensor's parameters are listed as Table 1.

TABLE 1. The sensor's parameters.

Range:	$0 \sim 110kPa$
Accuracy:	$0.2\%FSO$ $(optional: 0.1\%FSO)$
Output:	$4 \sim 20mA, 0 \sim 10V$
Power:	$24VDC$
Frequency response:	$1kHz(optional: 5kHz)$
Operating temperature range:	$-40 \sim 100^oC$
Compensation (accuracy) temperature range:	$-10 \sim 80^oC$

The pressure change in the cabin is recorded in Fig.21.

From the comparison between the experiment and the numerical calculation, Figure 21 and Figure 22 show the same trend on pressure change. It proves the mathematic model's correctness to some degree. Also, there is a large difference on time dimension between the numerical calculations and experimental results because of simplified physical model. This is particularly the case with perfect to the time evolution of the respective phenomena. But, it is not this paper's objective to pursue accurate simulation of the timeline. Further work need to be done to improve accuracy in this sense, and it is stated in Conclusion.

VI. CONCLUSION

In this paper, we calculate the conservative state equation (Eulerian equation) of flow field in the hyperbaric oxygen chamber by flux vector splitting computational format. And, the distribution of the parameters was obtained in the flow field. From the results of numerical calculation, the algorithm can capture transient distribution of the parameters of each time step from flowing start to its near stop. And, the flow direction and the pressure distribution is consistent with the expected in the flow field. In particular, this numerical calculation captured the shock wave during the supersonic air flow in hyperbaric oxygen chamber. Finally, it can be seen that the numerical results are consistent with the results of the actual flow from the experimental data in the trend of pressure change, as shown in Figures 21–22. This proves that numerical results have practical significance in predicting the trend of gas flow in hyperbaric oxygen chamber. And this proves that it can approach the real flow process well by using flux vector splitting algorithm to solve the Euler equation. Engineers and technicians can use this method to qualitatively simulate the flow of the flow field. The author's practice laid the foundation for the future use of this method to solve more complex flow field to replace the high cost experiment in hyperbaric oxygen chamber's designing.

Further work can be done to improve the accuracy of the model. First, a higher resolution calculation format should be applied, and the effects of thermal radiation and heat transfer should be added to the model. Second, some factors, which affect the calculation accuracy, need to be considered. They include the actual length of the pipe in the oxygen chamber, and include the effect of the pipe bend to gas flow, as shown in Figure 23. In the flow calculation, the effect of the items placed in the cabin should be taken into account on the air flow, as shown in Figure 19.

ACKNOWLEDGMENT

The author(s) declared no potential conflicts of interest with respect to the research, authorship, and/or publication of this article.

REFERENCES

[1] C. Alippi and A. D'Orazio, "Aerodynamic noise in hyperbaric chambers: Assessment and possible mitigation," *Acta Acustica United Acustica*, vol. 101, no. 1, pp. 174–180, 2015.

[2] S. Pietrowicz, P. Kolasiński, and M. Pomorski, "Experimental and numerical flow analysis and design optimization of a fume hood using the CFD method," *Chem. Eng. Res. Des.*, vol. 132, pp. 627–643, Apr. 2018.

[3] S.-K. Sun, X.-H. Jia, L.-F. Xing, and X.-Y. Peng, "Numerical study and experimental validation of a Roots blower with backflow design," *Eng. Appl. Comput. Fluid Mech.*, vol. 12, no. 1, pp. 282–292, 2018.

[4] A. Machold, L. Bürgler, A. Ennemoser, and M. Grubmüller, "Model-based combustion chamber layout for passenger car Diesel engines," in *Internationaler Motorenkongress*. Wiesbaden, Germany: Springer, 2017, pp. 315–339.

[5] Y. D. Kuan, J. M. Huang, J. H. Wong, C. Y. Chen, S. M. Lee, and C. N. Hsu, "Investigation of the flow and noise distribution on a blower via integration of simulation and experiments," *J. Mech.*, vol. 34, no. 2, pp. 151–158, 2017.
[6] A. Marsan and S. Moreau, "Aeroacoustic analysis of the tonal noise of a large-scale radial blower," *J. Fluids Eng.*, vol. 140, no. 2, 2018, Art. no. 021103.
[7] C. Liu and Z. Ji, "Computational fluid dynamics-based numerical analysis of acoustic attenuation and flow resistance characteristics of perforated tube silencers," *J. Vib. Acoust.*, vol. 136, no. 2, 2014, Art. no. 021006.
[8] S. Tan and Q. Li, "Time-implicit gas-kinetic scheme," *Comput. Fluids*, vol. 144, pp. 44–59, Feb. 2017.
[9] E. F. Toro and M. E. Vázquez-Cendón, "Flux splitting schemes for the Euler equations," *Comput. Fluids*, vol. 70, pp. 1–12, Nov. 2012.
[10] S. A. Tokareva and E. F. Toro, "A flux splitting method for the Baer–Nunziato equations of compressible two-phase flow," *J. Comput. Phys.*, vol. 323, pp. 45–74, Oct. 2016.
[11] Y. Chen, S. Jiang, and N. Liu, "HFVS: An arbitrary high order approach based on flux vector splitting," *J. Comput. Phys.*, vol. 322, pp. 708–722, Oct. 2016.
[12] F. Qu, C. Yan, D. Sun, and W. Yuan, "A parameter-free upwind scheme for all speeds' simulations," *Sci. China Technol. Sci.*, vol. 58, no. 3, pp. 434–442, 2015.
[13] C. Brehm, C. Hader, and H. F. Fasel, "A locally stabilized immersed boundary method for the compressible Navier–Stokes equations," *J. Comput. Phys.*, vol. 295, pp. 475–504, Aug. 2015.
[14] X. An and M. Xu, "Nonlinear panel flutter analysis based on an improved CFD/CSD coupled procedure," *Comput. Model. Eng. Sci.*, vol. 98, no. 6, pp. 601–629, 2014.
[15] J. D. Anderson, Jr., *Computational Fluid Dynamics the Basics With Applications*, 1st ed. New York, NY, USA: McGraw-Hill, 1995, pp. 77–78.
[16] E. G. Sinaiski, *Hydromechanics: Theory and Fundamentals*. Hoboken, NJ, USA: Wiley, 2011.
[17] C. Hirsch, *Numerical Computation of Internal and External Flows: Computational Methods for Inviscid and Viscous Flows*, vol. 2. Chichester, U.K.: Wiley, 1990, pp. 144–145.
[18] R. Courant, K. Friedrichs, and H. Lewy, "Über die partiellen Differenzengleichungen der mathematischen Physik," *Math. Ann.*, vol. 100, no. 1, pp. 32–74, 1928.

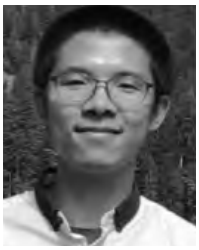

LIN LI received the B.S. degree in mechanical engineering from the North University of China, Taiyuan, Shanxi, China, in 2011, and the M.S. degree in mechanical engineering from Guizhou University, Guiyang, China, in 2015. He is currently pursuing the Ph.D. degree in mechanical engineering with the Beijing Institute of Technology, Beijing, China. From 2016 to 2018, he was a Visiting Scholar with the Texas A&M University, College Station, TX, USA. His research interests include vehicle dynamic and control, hybrid electric vehicle energy management, intelligent transportation system, computational fluid dynamic, and macroscopic traffic flow model.

JUNQIANG XI received the B.S. degree in automotive engineering from the Harbin Institute of Technology, Harbin, China, in 1995, and the Ph.D. degree in vehicle engineering from the Beijing Institute of Technology (BIT), Beijing, China, in 2001. In 2001, he joined the State Key Laboratory of Vehicle Transmission, BIT. From 2012 to 2013, he made research as an advanced Research Scholar with the Vehicle Dynamic and Control Laboratory, The Ohio State University (OSU), Columbus, OH, USA. He is currently a Professor and the Director of the Automotive Research Center, BIT. His research interests include vehicle dynamic and control, power-train control, mechanics, intelligent transportation systems, and intelligent vehicles.

REZA LANGARI (SM'02) received the B.Sc., M.Sc., and Ph.D. degrees from the University of California, Berkeley, CA, USA, in 1981, 1983, and 1991, respectively. He was with Measurex Corporation (1984–1995); Integrated Systems, Inc. (1985–1986); and Insight Development Corporation (1987–1989), prior to starting his academic career with Texas A&M University, College Station, TX, USA, in 1991. Since then, he has held research positions with the National Aeronautics and Space Administration Ames Research Center, the Rockwell International Science Center, the United Technologies Research Center, and the U.S. Air Force Research Laboratory. His expertise is in the area of computational intelligence, with application to mechatronic systems, industrial automation, and automated vehicles. He has co-authored *Fuzzy Logic: Intelligence, Control and Information* (Prentice Hall, 1999) and *Measurement and Instrumentation* (Elsevier, 2011, 2015, 2nd ed.). He has co-edited the *Fuzzy Control: Synthesis and Analysis* (Wiley, 2000) and the *Industrial Applications of Fuzzy Systems* (IEEE Press, 1995). He has served as an Associate Editor for the IEEE TRANSACTIONS ON FUZZY SYSTEMS, the IEEE TRANSACTIONS ON VEHICULAR TECHNOLOGIES, and the *ASME Journal of Dynamic Systems, Measurement, and Control*. He currently serves as the Editor-in-Chief of the *Journal of Intelligent and Fuzzy Systems* (IOS Press, The Netherlands).